

Cite this: *J. Mater. Chem. A*, 2019, 7, 21730

Highly efficient and stable perovskite solar cells via bilateral passivation layers†

Tun Wang,  Zhendong Cheng, Yulin Zhou, Hong Liu* and Wenzhong Shen*

NiO_x-based perovskite solar cells (PSCs) have drawn tremendous attention and achieved significant improvement in recent years. Interfacial engineering is a promising route for enhancing performances of PSCs with larger open-circuit voltage (V_{OC}) and short-circuit current density (J_{SC}). Herein, we report a simple method for improving the performance of PSCs by applying bilateral polystyrene layers between the perovskite absorber and charge transport layers, respectively. The top and bottom surfaces of the perovskite layer are passivated and protected by ultrathin bilateral polystyrene layers, which results in highly efficient devices with a larger perovskite grain size, fewer interfacial defects and suppressed charge recombination. As a result, a power conversion efficiency (PCE) of 19.99% is achieved without hysteresis and the V_{OC} is as high as 1.149 V, which is so far the best result for p-i-n PSCs based on pure CH₃NH₃PbI₃. Moreover, the devices also show improved long-term stability. This study provides a powerful strategy to design and prepare highly efficient and stable perovskite solar cells.

Received 25th July 2019
Accepted 30th August 2019

DOI: 10.1039/c9ta08084h

rsc.li/materials-a

1. Introduction

Perovskite solar cells (PSCs) have attracted much attention because of their desirable advantages such as the simple fabrication process, adjustable band energy, efficient light absorption, high charge-collection efficiency, *etc.*^{1,2} The record power conversion efficiency (PCE) has rapidly increased to over 24% in recent years, making them potential candidates for new generation photovoltaic technology in the near future.^{3–5} To achieve high-performance PSCs, all of the functional layers in a perovskite solar cell have to be successively prepared as perfectly as possible by controlling both morphological and electronic properties because each layer plays a vital role in the device performance.⁶ Recently, as an outstanding representative of p-type metal oxide semiconductors, nickel oxide (NiO_x) has been extensively studied as a hole transport layer (HTL) because of its suitable work function, high conduction band edge, high electrical conductivity, and high thermal and chemical stability^{7,8} and can be an excellent replacement for the popular organic HTL materials, such as Spiro-OMeTAD and PEDOT:PSS.^{9–11} The hysteresis of PSCs based on an NiO_x HTL can be effectively suppressed using inverted planar configuration (p-i-n) compared with the normal n-i-p architecture.^{12,13} This is due to the limited ion migration, balanced hole and electron transport efficiency, and appropriate compensation for

the slightly shorter diffusion length of holes than of electrons in the perovskite film for the inverted heterojunction devices.^{10,14} However, it is still challenging to prepare highly efficient and stable PSCs. Firstly, the organic-inorganic hybrid perovskite material CH₃NH₃PbI₃ (MAPbI₃) is very sensitive to humidity and heat, which significantly degrade the photovoltaic properties and stability of the prepared PSCs when they are exposed to a hot and humid environment.¹⁵ Secondly, the pinholes or crystal defects of a prepared perovskite layer induced by grain boundaries and roughness cannot be easily removed by solution-derived methods even though the preparation process has been significantly optimized. This would enhance the non-radiative recombination and thus cause a loss in open-circuit voltage (V_{OC}) and short-circuit current density (J_{SC}).¹⁶ What's more, the weak chemical interaction at the perovskite/NiO_x interface may also limit the efficiency of the device.^{17,18} It has been reported that the photoinduced carriers can penetrate through the perovskite layer without significant charge recombination.¹⁹ Therefore, enhancing the contact and transport of carriers at the interfaces of perovskite/charge transport layers and minimizing the charge recombination has become increasingly significant.

Recently, several approaches have been proposed to reduce interfacial defects and achieve higher V_{OC} in optimized devices.^{20,21} Interfacial passivation has been developed from the point of view of perovskite grain boundary and interface modification, such as by adding insulating polymers,^{19,22–24} ethanolamine molecules²⁵ or organic salt^{26,27} to cap perovskite layers. However, this approach only blocks photogenerated charge recombination on one side of the perovskite layer, which may aggravate the charge-carrier imbalance because of

Key Laboratory of Artificial Structures and Quantum Control (Ministry of Education), Institute of Solar Energy, School of Physics and Astronomy, Shanghai Jiao Tong University, Shanghai 200240, P. R. China. E-mail: liuhong@sjtu.edu.cn; wzshen@sjtu.edu.cn

† Electronic supplementary information (ESI) available. See DOI: 10.1039/c9ta08084h

asymmetric charge extraction in the HTL and electron transport layer (ETL).²² Besides, the interfacial recombination centers cannot be effectively reduced in the other unprotected interface. For this sake, double-side passivation using poly(methyl methacrylate) (PMMA) was proposed by White *et al.* and a PCE of 20.8% based on multi-cation perovskite was achieved.²⁸ However, their device structure and manufacturing processes were quite complicated, and the interfacial passivation mechanism was not fully discussed and understood. They inserted a mixed PCBM/PMMA film between perovskite and the ETL as the passivation layer and did not explain their respective functions. Besides, it was not clear how the thickness of the passivation layer influences the photovoltaic performances of the PSCs.

In this work, we utilize polystyrene (PS) as a passivation medium to modify the surface of an electrochemically deposited NiO_x film to improve perovskite quality. Furthermore, PS mixed in chlorobenzene (CB) is used as an antisolvent to slow down perovskite crystal growth and fill the traps among perovskite grains on top. The utilization of bilateral passivation layers can lead to the efficient passivation of trap states at perovskite/HTL and perovskite/ETL interfaces. In the meantime, photogenerated holes and electrons can pass through the bilateral passivation layers *via* the tunneling effect from the perovskite absorber to the HTL and ETL, respectively, while they are blocked in the inverse directions, thereby increasing the V_{OC} and J_{SC} without distinctly sacrificing the fill factor (FF). Consequently, the p-i-n PSCs with a structure of $\text{FTO}/\text{NiO}_x/\text{PS}/\text{MAPbI}_3/\text{PS}/\text{PCBM}/\text{Ag}$ exhibits a PCE of 19.99% with a high V_{OC} of 1.149 V. This has been the highest value for solar cells based on pure MAPbI_3 and an NiO_x HTL so far. Furthermore, the bilaterally passivated devices show better long-term stability than those without passivation layers. The results in this study suggest that bilateral passivation for a perovskite film is an effective procedure to improve the performances of PSCs and it also has potential applications in developing light-emitting diodes based on perovskite materials.

2. Results and discussion

To investigate the effect of interfacial passivation on the photovoltaic performance of PSCs, planar inverted PSCs were prepared with different procedures as described in the Experimental section and the procedures for preparing perovskite films are shown in Fig. 1. For preparing the perovskite film with a bottom passivation layer, the PS/CB solution was first spin-coated on the NiO_x film and then the perovskite film was grown on the bottom PS film using CB as the antisolvent (P1). For preparing the bilaterally passivated perovskite film, the PS/CB solution was first spin-coated on the NiO_x film and then the perovskite film was grown on the bottom PS film using the PS/CB solution as the antisolvent. Naturally, the perovskite film was covered by the top PS film (P2). The reference sample was prepared by directly spin-coating the perovskite precursor on the NiO_x film, in which pure CB was applied as the antisolvent (P3). As a result, samples with structures of $\text{FTO}/\text{NiO}_x/\text{PS}/$

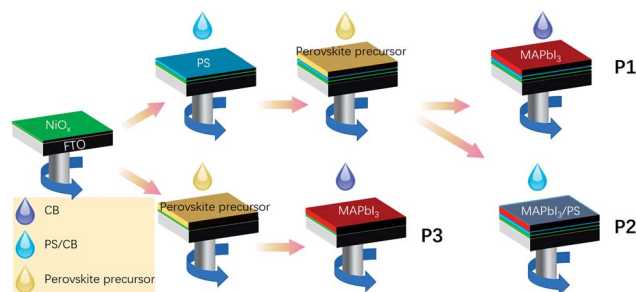


Fig. 1 Schematic illustration of the procedures for preparing perovskite films with and without passivation layers. P1: procedure for the preparing perovskite film with a bottom passivation layer. P2: procedure for preparing the bilaterally passivated perovskite film. P3: procedure for preparing the perovskite film without a passivation layer.

MAPbI_3 , $\text{FTO}/\text{NiO}_x/\text{PS}/\text{MAPbI}_3/\text{PS}$ and $\text{FTO}/\text{NiO}_x/\text{MAPbI}_3$ were obtained by P1, P2 and P3, respectively.

After depositing the passivation film with different PS concentrations, the mesoporous NiO_x film was gradually covered by the PS passivation layer with increasing concentrations of the PS solution from 0.2 to 2.0 mg mL^{-1} (can be seen in Fig. S1 in the ESI†). Notably, all the samples exhibit high optical transmittance around 85% in the visible range, almost the same as with the bare FTO substrate, suggesting that the passivation layer has negligible influence on the optical transmittance (Fig. 2a). Such a high transparency would be a necessary prerequisite for preparing highly efficient PSCs.²⁹ However, the wettability measurement has shown a significant variation of surface tension with the PS concentration. As shown in Fig. 2b, the contact angle of the pristine sample without the PS passivation layer was 41.5° , and it dramatically increased to 95.9° with the PS layer at the concentration of 2.0 mg mL^{-1} . The enhanced non-wetting properties can significantly reduce the surface tension dragging force applied on the perovskite film according to a previous report,³⁰ thus resulting in higher grain boundary mobility and larger grains.

The grain size and surface roughness of perovskite films with or without passivation treatment were characterized *via* scanning electron microscopy (SEM) and atomic force microscopy (AFM). Fig. 3a–c show the images of the perovskite film deposited on the bottom passivation film. The perovskite film shows compact and uniform morphology with closely packed grain boundaries. Notably, the perovskite grain size is

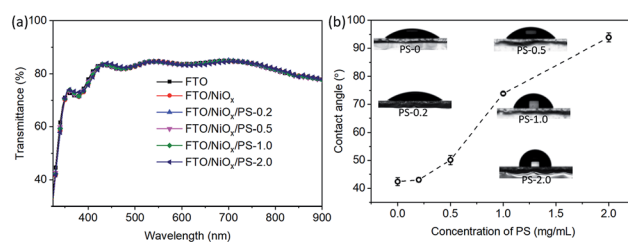


Fig. 2 (a) Optical transmission spectra and (b) surface contact angles of the FTO/NiO_x samples deposited with different concentrations of PS. The numbers represent the PS concentration in mg mL^{-1} .

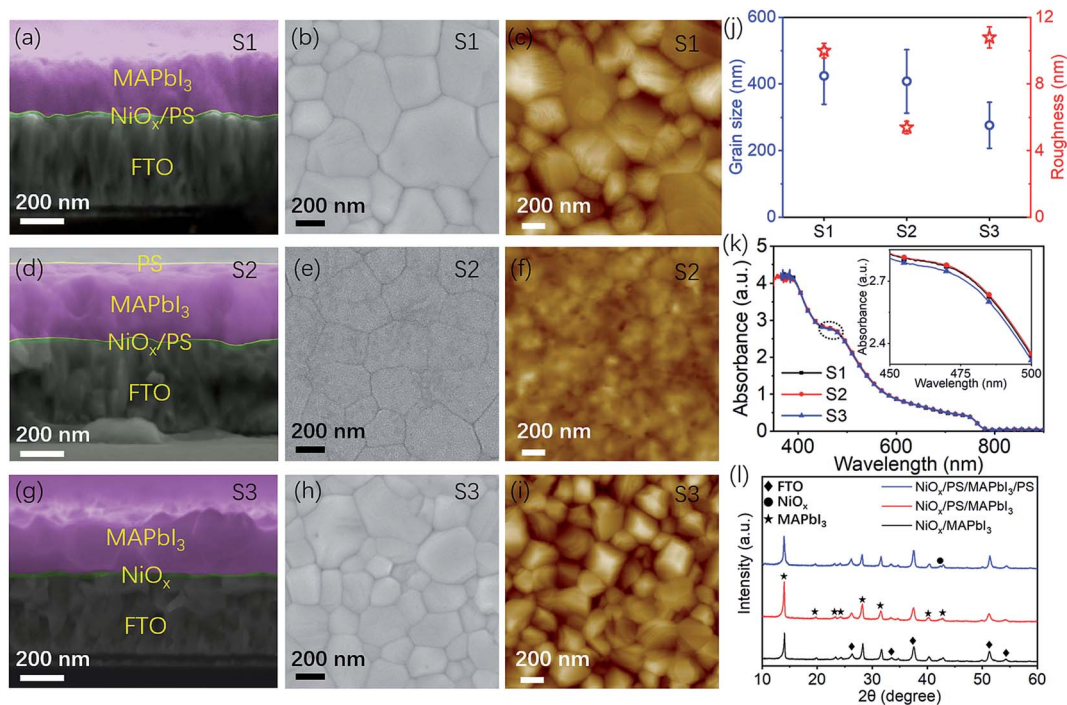


Fig. 3 Cross-sectional and top-view SEM and AFM images of perovskite layers with (a–c) bottom passivation (S1) and (d–f) bilateral passivation layers (S2) and (g–i) without passivation layers (S3). (j) Statistical distribution of the grain size and surface roughness of the corresponding samples. (k) Optical absorption spectra of the corresponding samples. (l) XRD patterns of perovskite films deposited on different films. The characteristic peaks of FTO, NiO_x and perovskite are indicated by diamonds, circles and stars, respectively.

significantly affected by the PS concentration when preparing perovskite bottom passivation layers and the largest average grain size is observed at a PS concentration of 0.5 mg mL⁻¹ (Fig. S2a†). The increased grain size is ascribed to the non-wetting and smoother surface of the substrate with lower surface tension as discussed in Fig. 2b. The perovskite films with large grain sizes and no pinholes are crucial for reducing charge recombination, which can guarantee the effective extraction and transport of photoinduced carriers from the perovskite active layer to the corresponding charge transport layer.³¹ For further studying the effect of bilateral passivation layers, the perovskite film was deposited on the bottom passivation layer with PS-0.5 (the number represents the PS concentration in mg mL⁻¹). Similarly, the PS solution acted as the antisolvent during the spin-coating process. In this case, the perovskite layer was capped by the bottom and top passivation layers. As the antisolvent, the PS concentration had a significant influence on the surface roughness of the deposited perovskite film, but not the grain size (Fig. S2b†). As can be seen in Fig. 3d–f, the perovskite film with bilateral passivation layers exhibits a much smoother surface and closer grain boundaries compared to the sample with only the bottom passivation layer (Fig. 3a–c) and the reference sample without passivation layers (Fig. 3g–i). The statistics of the grain size and surface roughness of the optimal perovskite film prepared by different processes are shown in Fig. 3j (for clarity, S1 represents the perovskite film deposited on the bottom passivation layer and shows a structure of FTO/NiO_x/PS/MAPbI₃, while S2 and S3 represent FTO/NiO_x/PS/

MAPbI₃/PS and FTO/NiO_x/MAPbI₃, respectively). The perovskite films with bottom passivation (S1) and bilateral passivation layers (S2) exhibit a layer average grain size (~430 nm) compared to the reference sample without passivation (S3). In particular, the mean surface roughness of the prepared perovskite film sharply decreases from ~10 nm to ~5 nm after applying the PS solution as the antisolvent, which clearly indicates that the solution-processed PS layer fills the tiny pinholes and grain boundaries of the perovskite film. This contributes to flatter and more compact perovskite films with a top passivation layer, thereby enabling better contact between the electron transport layer (ETL) and the perovskite photoactive layer.³²

Fig. 3k shows the optical absorption spectra of the perovskite films with bottom and bilateral passivation layers and without passivation layers. The features of the absorption spectra are almost the same because the PS film exhibits extremely high transparency in the visible and near-infrared regions.³³ The inset clearly shows that S1 and S2 have similar optical absorbance, which is slightly higher than that of the reference sample S3. The enhanced absorption could be ascribed to the improved morphology and larger grain size of the perovskite film according to the previous literature.³¹ The X-ray diffraction (XRD) diagram gives further insight into the influence of passivation layers on the crystal structure and morphology of the prepared perovskite films. As shown in Fig. 3l, the typical characteristic peaks of MAPbI₃ are clearly observed (indicated by stars) and no other residual peaks were found, suggesting high purity and quite good crystallization in the perovskite film.

Besides, the peak located at 14.1° should be assigned to the (110) plane of the MAPbI₃ film deposited on the NiO_x/PS film³⁴ and shows a relatively stronger intensity than that of the reference sample and bilaterally passivated perovskite films, demonstrating better crystallinity of perovskite.

To study the results of the evolution described above, we have carried out steady-state photoluminescence (PL) and time-resolved PL (TRPL) measurements for the effect of passivation on the charge transfer efficiency from the perovskite photoactive layer to the NiO_x HTL. Since the PL intensity can be very sensitive to the focal point on the perovskite film,³⁵ we have performed repeated measurements to avoid this effect by fine tuning the position of the samples on the z-axis and chosen the optimal spectrum with the largest PL peak intensity for each sample. As shown in Fig. 4a, the reference sample with an architecture of NiO_x/MAPbI₃ displays a very strong perovskite emission peak near 764 nm, while it remarkably decreases for the sample of NiO_x/PS/MAPbI₃ without a significant shape change. It is generally recognized that the lower PL intensity means higher PL quenching and more efficient charge separation at the perovskite/HTL interface.³⁶ Therefore, the perovskite film with a bottom PS passivation layer exhibits an enhanced hole extraction capability compared with the reference sample. Besides, the PL peak of the perovskite film with a bottom PS passivation layer exhibits a small redshift to 766 nm, indicating a wider range and stronger absorption because of the enlarged perovskite grain size.³⁷ Nevertheless, the perovskite film wrapped by the bilateral PS layers (NiO_x/PS/MAPbI₃/PS) shows a stronger PL intensity compared with the sample with only the bottom PS passivation layer. This result might have arisen from the improved perovskite film quality due to surface and boundary passivation on the voids and grain boundaries of the

perovskite layer,³⁸ which would distinctly reduce the surface roughness of the perovskite layer, as described in Fig. 3. The TRPL examination was further implemented to investigate the interfacial charge transport properties. Fig. 4b shows the corresponding TRPL spectra of the MAPbI₃ films with and without passivation layers. The PL decay scatters were fitted with a biexponential decay function $I = A_1 \exp(-(t - t_0)/\tau_1) + A_2 \exp(-(t - t_0)/\tau_2) + I_0$, where A_1 and A_2 are the relative weighting coefficients and τ_1 and τ_2 are the lifetimes for the fast and slow recombination, respectively.³⁹ As can be seen from the extracted parameters in Table 1, the reference sample of NiO_x/MAPbI₃ has a fast-decay lifetime of $\tau_1 = 5.8$ ns and a slow-decay lifetime of $\tau_2 = 24.1$ ns. In contrast, NiO_x/PS/MAPbI₃ gives $\tau_1 = 3.6$ ns and $\tau_2 = 11.7$ ns, respectively. This demonstrates that charge extraction can be significantly enhanced after introducing the passivation layer between the NiO_x HTL and perovskite absorber.²² Accordingly, the PL intensity of perovskite with bilateral passivation layers (NiO_x/PS/MAPbI₃/PS) shows a weaker quenching effect in comparison to that of the bottom passivation layer-based sample, where the fast-decay and slow-decay lifetimes are 4.3 and 12.8 ns, respectively. The increase in PL intensity and lifetime for the bilaterally passivated perovskite films may be attributed to the improvement of

Table 1 Summary of the fitted parameters of the TRPL decay traces

Structure	A_1 (%)	τ_1 (ns)	A_2 (%)	τ_2 (ns)	τ_a (ns)
NiO _x /MAPbI ₃	70.4	5.8	29.6	24.1	17.4
NiO _x /PS/MAPbI ₃	89.6	3.6	10.4	11.7	5.8
NiO _x /PS/MAPbI ₃ /PS	68.8	4.3	31.2	12.8	9.2

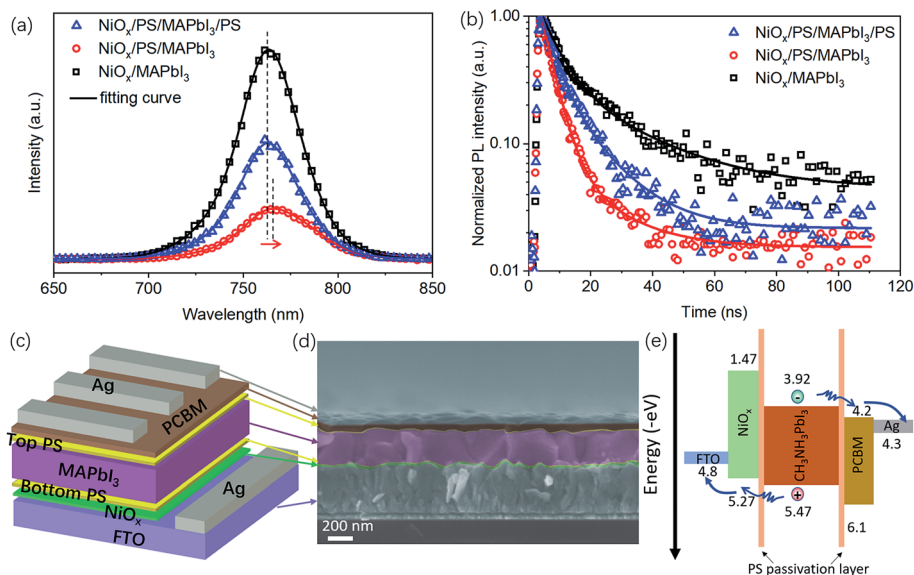


Fig. 4 (a) Steady-state photoluminescence (PL) and (b) time-resolved PL spectra of perovskite films under different layer passivation conditions. Solid lines in (a) and (b) are curves fitted by Gaussian and double exponential functions, respectively. (c) Three-dimensional schematic architecture and (d) false color cross-sectional SEM image of a typical MAPbI₃ solar cell bilaterally passivated by PS layers. (e) Schematic representation of the energy band diagram for the PSC device.

perovskite film properties such as the reduction of surface roughness and the filling of voids and grain boundaries by the top PS film. As a result, the interfacial recombination and charge trapping loss could both be suppressed at the interfaces, and thus the V_{OC} can be significantly improved.^{16,28,32}

Next, the PCBM layer and silver electrodes were sequentially deposited onto the perovskite films to form typical p-i-n type PSCs, as shown in Fig. 4c. The false color cross-sectional SEM image of a completed solar cell device shown in Fig. 4d exhibits uniform layer formation and quite regular interfacial conditions. The energy band diagram of the prepared PSC is shown in Fig. 4e according to the optical bandgap, work function and valence band maximum (VBM) edge of prepared NiO_x in our previous report.³⁹ The energy levels of FTO, NiO_x , MAPbI₃, PCBM, and Ag are all well aligned under vacuum. As tunneling channels, the PS layers can selectively conduct one type of charges while blocking the other type because the charge selective electrodes and carrier transport layers have a suitable electronic state with matching energy levels for each type of carrier.^{19,40} What's more, the perovskite grain boundaries can be filled by the PS material on the top, which will be beneficial for suppressing the charge recombination at the interface and passivating the interface to increase device performance.

Furthermore, the photovoltaic performance of these PSCs was studied in detail. Fig. 5a shows the photocurrent–voltage (J – V) curves of the perovskite devices with bottom passivation

layers of different thicknesses which were adjusted by changing the concentration of the PS solution in the spin-coating process. The reference device without PS passivation layers exhibits typical photovoltaic performance with a V_{OC} of 1.050 V, a J_{SC} of 21.06 mA cm⁻², an FF 71.74% and a PCE of 15.87%. Amazingly, after introducing the PS passivation layer between perovskite and the NiO_x HTL, the fabricated PSCs exhibited great improvement. For example, the V_{OC} and J_{SC} increased to 1.108 V and 22.45 mA cm⁻². It should be mentioned that the performance of the perovskite devices with the bottom passivation layer can be significantly affected by the passivation thickness, which was tuned by PS concentration. For example, when the PS concentration is increased to 0.2, 0.5, 1.0 and 2.0 mg mL⁻¹, the PCE increased to 16.82%, 18.39%, 17.96% and 14.49%, respectively (detailed parameters and the corresponding statistical distributions are summarized in Table S1 and Fig. S3b in the ESI†). Fig. S3a† shows the three-dimensional (3D) architecture of the bottom-passivated PSC device. The champion devices with the bottom passivation layer fabricated with a 0.5 mg mL⁻¹ PS concentration exhibited an average V_{OC} of 1.108 V, a J_{SC} of 22.45 mA cm⁻², an FF 73.94% and a PCE of 18.39%. The increased J_{SC} and V_{OC} could be attributed to the larger perovskite grain size shown in Fig. 3 and fewer defects at the HTL/perovskite interface due to the interfacial passivation effect.²⁶ The statistical distribution in Fig. S3b† also shows a similar trend. Further increasing the PS concentration to

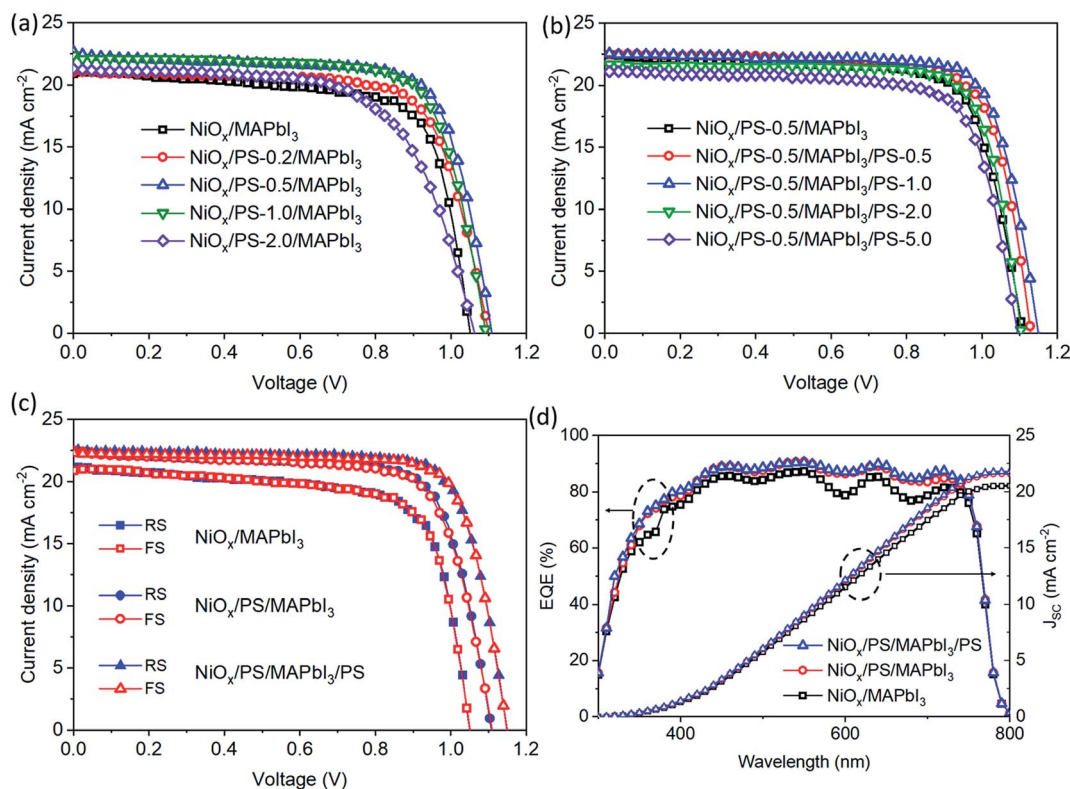


Fig. 5 (a) J – V curves of PSCs based on the bottom passivation layer with different PS concentrations. (b) J – V curves of bilaterally passivated PSCs with different PS concentrations for the top passivation layer. (c) J – V curves of the champion PSCs prepared from pristine perovskite, bottom-passivated perovskite and bilaterally passivated perovskite, measured in both reverse and forward directions. RS – reverse scanning, FS – forward scanning. (d) EQE spectra of the corresponding PSCs.

2.0 mg mL⁻¹ can seriously degrade the V_{OC} , J_{SC} , FF and PCE to 1.062 V, 21.22 mA cm⁻², 64.31% and 14.49%, respectively. A possible reason is that very high passivation layer thickness would greatly weaken the tunneling effect and the conductivity, and therefore degrade the device performance.¹⁹

To further study the effect of the bilateral passivation layers on the PSCs, we deposited the perovskite film onto the NiO_x/PS film under optimum conditions (0.5 mg mL⁻¹ PS) by a one step method, and the PS dissolved in CB solution was applied as the antisolvent during the spin-coating process. The measured J - V curves of PSCs with different concentrations of antisolvent are shown in Fig. 5b. Similarly to the bottom passivation layer, the top passivation layer thickness also exhibits a significant influence on the performance of the prepared devices (detailed photovoltaic parameters and statistics are summarized in Table S2 and Fig. S3d†). When the PS concentration is increased from 0 to 0.5 and 1.0 mg mL⁻¹, the V_{OC} remarkably improved from 1.108 V to 1.129 V and 1.149 V, respectively, and the FF increased from 73.94% to 75.44% and 77.33%, respectively. When the PS concentration is larger than 1.0 mg mL⁻¹, all the photovoltaic parameters display a non-negligible decrease, which can also be ascribed to the obstruction of charge tunneling as discussed above.

As shown in Fig. 5c, the negligible hysteresis of the J - V curves was not suppressed after inserting PS layers. Table 2 displays all the parameters of the PSCs prepared from pristine, bottom-passivated and bilaterally passivated perovskite in both reverse and forward voltage scanning directions. The champion device with bilateral passivation layers shows a PCE of 19.99% and 19.88% for the reverse and forward scan, respectively. It is worth noting that the PSCs based on the bilaterally passivated perovskite film show a very high V_{OC} of 1.149 V, which is so far the closest recorded value to the Shockley–Queisser theoretical limit value of ≈ 1.30 V for pure PSCs based on the NiO_x HTL.⁴¹ As far as we know, this is the largest value for the pure MAPbI₃-based device in experiments (details can be found in Table S3 in the ESI†).^{42,43} Moreover, the external quantum efficiency (EQE) spectra in Fig. 5d exhibit the details of the improved photovoltaic performance of PS passivated PSCs from the spectroscopic response. Compared to the reference device without passivation layers, the EQE spectra for both bottom-passivated and bilaterally passivated samples are gradually enhanced and exhibit broad plateaus around 90% in the range of 450–750 nm. The integrated J_{SC} of the champion device can increase up to 21.80 mA cm⁻², which is comparable with the measured J_{SC} of 22.51 mA cm⁻² shown in Table 2.

Fig. 6a presents the statistics of photovoltaic parameters V_{OC} and J_{SC} for over 30 devices under different conditions. The significantly increased J_{SC} and V_{OC} for the bilaterally passivated devices could be attributed to the fewer defects at HTL/perovskite and ETL/perovskite interfaces and suppressed carrier recombination.¹⁹ The statistics of PCE in Fig. 6b demonstrate the reliability and the repeatability of the performance enhancement by the passivation effect. The majority of PCE values for the bilaterally passivated devices are located around $\sim 19\%$, consistent with the above result shown in Fig. S3.† Electrochemical impedance spectroscopy (EIS) was conducted to examine the details of charge transport and interface resistance and further understand the roles of the passivation layers in the solar cell devices. The Nyquist plots shown in Fig. 6c display a remarkable change in the radius of the curves with similar shapes. In this experiment, only the semicircle for the high frequency response can be observed, which is related to the recombination processes according to the literature.¹⁸ Generally, a larger arc corresponds to a higher recombination resistance (R_{rec}).³² As can be seen from the curve, the R_{rec} of the PSCs based on the PS passivation layer is much higher than that of the reference device. This is consistent with the previous results of V_{OC} . Capacitance–voltage (C - V) characterization was subsequently conducted under dark conditions to examine the junction properties at the interfaces of the HTL/perovskite and ETL/perovskite. Deduced from Mott–Schottky impedance analysis (Fig. 6d), the built-in potential (V_{bi}) for the PSCs based on bottom and bilateral PS passivation layers is 1.00 V and 1.11 V, respectively, which are much higher than that of the reference device (0.94 V) without passivation layers. The enhanced V_{bi} could facilitate charge extraction and avoid the charge accumulation at the interfaces between perovskite and charge transport layers, and improve photovoltaic performance of PSCs.⁴⁴

The main contribution to the PCE increase comes from the enhancement of V_{OC} and J_{SC} , which may also be attributed to the optimization of trap densities of devices owing to the inserted bilateral passivation layers. As shown in Fig. 7a, the space-charge limited current (SCLC) method was carried out to detect the defect states in the perovskite layers. The J - V curves of the hole-only devices (FTO/NiO_x(/PS)/MAPbI₃(/PS)/Ag) can be divided into three distinct regions: an ohmic region (the linear interval to the left), a trap-filling limited (TFL) region (the steep rising interval in the middle) and a trap-free SCLC region (the curved portion to the right).⁴⁵ The trap-filling limited voltage (V_{TFL}) indicates the transition from the ohmic region to the TFL

Table 2 Photovoltaic parameters of the PSCs with or without PS passivation layers

Structure	Scan direction	V_{OC} (V)	J_{SC} (mA cm ⁻²)	FF (%)	PCE (%)
NiO _x /MAPbI ₃	Reverse	1.050	21.11	71.74	15.90
	Forward	1.050	21.06	71.56	15.82
NiO _x /PS/MAPbI ₃	Reverse	1.108	22.45	73.94	18.39
	Forward	1.109	22.43	73.25	18.22
NiO _x /PS/MAPbI ₃ /PS	Reverse	1.149	22.51	77.33	19.99
	Forward	1.148	22.25	77.84	19.88

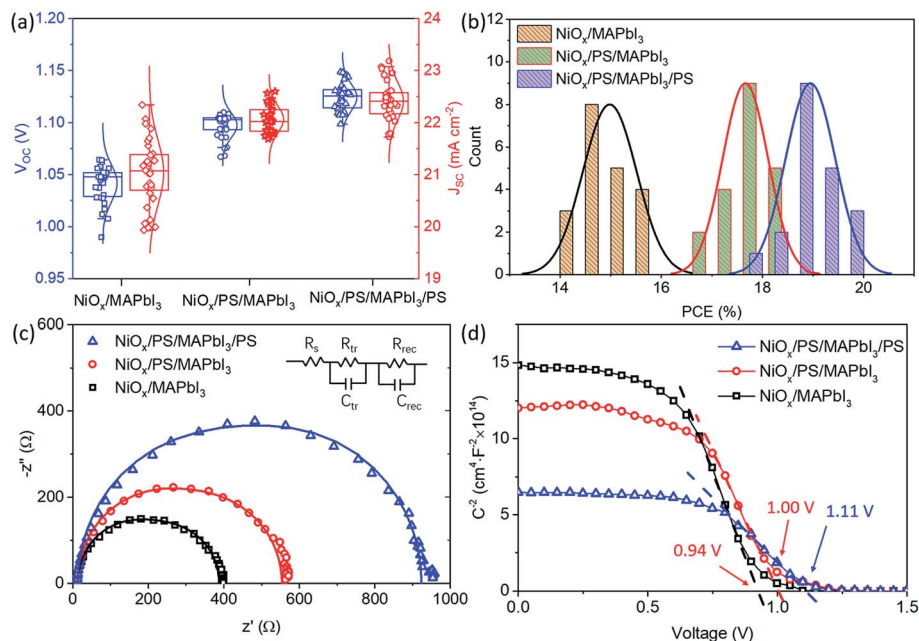


Fig. 6 (a) Statistics of V_{oc} and J_{sc} and (b) PCE distribution histogram for the bottom-passivated, bilaterally passivated and reference PSCs. (c) Nyquist plots of impedance and (d) Mott-Schottky curves for the bottom-passivated, bilaterally passivated and reference PSCs.

region, and can be used to calculate the trap-state density (n_{trap}) at the perovskite/HTL interface according to the relationship $V_{TFL} = qn_{trap}L^2/2\epsilon\epsilon_0$ (where q is the elementary charge, L is the

thickness of the hole-only device (~ 500 nm), ϵ is the relative dielectric constant of $MA\text{PbI}_3$ perovskite (6.5), and ϵ_0 is the vacuum permittivity).⁴⁶ The V_{TFL} values of the pristine planar

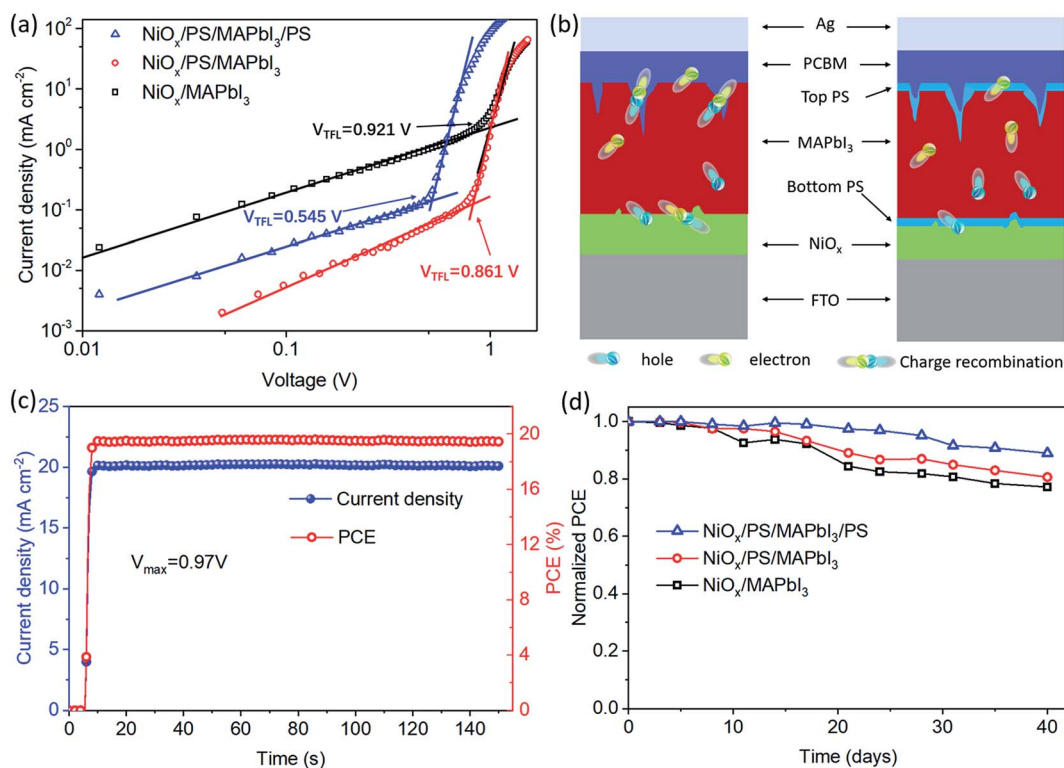


Fig. 7 (a) Dark $J-V$ curves of the hole-only devices. (b) Schematics of the carrier dynamics model in PSCs without (left) and with (right) bilateral passivation layers. (c) Steady-state photocurrent of the champion device measured at a bias voltage (0.97 V) near the maximum power point and the corresponding calculated PCE. (d) Normalized PCE of the reference device without passivation layers and the bilaterally passivated PSC device as a function of storage time.

perovskite and the bottom-passivated and bilaterally passivated perovskite films are 0.921, 0.861 and 0.545 V, respectively. As a result, the derived n_{trap} is reduced from $2.65 \times 10^{15} \text{ cm}^{-3}$ for the pristine perovskite film to 2.48×10^{15} and $1.57 \times 10^{15} \text{ cm}^{-3}$ for the bottom-passivated and bilaterally passivated perovskite films, respectively. Therefore, introducing the bilateral PS passivation layers is beneficial for reducing trap recombination at the HTL/perovskite interface. As shown in Fig. 7b, the schematic diagram of the photo-induced carrier dynamics in the PSCs can further explain why the solar cells based on bilaterally passivated perovskite (right) show better performances than the reference sample without the passivation layer (left). The advantages of the bilateral passivation effect can be summarized in the following three aspects. Firstly, the bottom passivation layer increases the grain size of perovskite, which enhances its light absorption ability. Secondly, the top passivation layer fills the pinholes and grain boundaries, which results in a smoother perovskite film with fewer interfacial defects. Finally, the top and bottom passivation layers isolate the MAPbI₃/ETL and MAPbI₃/HTL, respectively, reducing the recombination losses and shunt-leak current paths.³⁸ As a consequence, the bilaterally passivated PSCs exhibit better photovoltaic performance than the reference devices and the single-side passivated samples. Fig. 7c shows the steady photocurrent and PCE measured at the maximum power output point (0.97 V) of the champion device with bilateral passivation layers. The quickly stabilized PCE and the steady photocurrent measured at the maximum power point agree well with the results in Fig. 5c, which also supports the successful suppression of hysteresis in our PSCs.

Moreover, considering the sandwich-like configuration of bilateral passivation layers and the perovskite layer, the stability of the PSCs should also be interesting to evaluate. We therefore monitored the long-term stability of fabricated PSCs without encapsulation stored in a drying cabinet with an ambient atmosphere in the dark (temperature of ~ 22 °C and relative humidity of $\sim 2\%$) and the J - V characteristics were periodically recorded to extract the photovoltaic parameters. As shown in Fig. 7d, the reference device without passivation layers retains 77% of its initial efficiency after 40 days of storage, which is consistent with the previous reports.^{47,48} After introducing the passivation layer between the perovskite and carrier transport layers, the stability of the devices was significantly improved. In particular, the devices with bilateral passivation layers retain 89% of the original efficiency after 40 days of storage. The thermal stability of the perovskite films with or without passivation layers was also characterized in an ambient environment. The pristine perovskite film became completely decomposed after 90 min of heating at 120 °C in ambient air (humidity 60%), while the single-side passivated perovskite film exhibited a slower decomposition rate, and the bilaterally passivated one remained stable under the same conditions (detailed images can be found in Fig. S4 in the ESI†). The improved long-term and thermal stability of the perovskite film with bilateral passivation layers could possibly be ascribed to the suppression of morphological defects due to the passivation effect on the perovskite/ETL (or HTL) interfaces, which promotes the real application of PSCs.

3. Conclusion

We have developed a strategy to improve both the efficiency and stability of inverted planar PSCs with a PCE of 19.99% and a V_{OC} of 1.149 V by inserting bilateral PS films on the double-surface of the perovskite layer. The ultrathin PS films work as passivation layers, which suppress the carrier recombination and shunt-current leakage at interfaces between perovskite and charge transport layers. Moreover, the bilaterally passivated devices exhibited excellent long-term and thermal stability. Our studies indicate that bilateral passivation may be an effective enhancement method for efficient and stable PSCs in general and would have potential applications in other film-based electronic devices as well.

4. Experimental section

4.1. Materials

Methylammonium iodide (CH₃NH₃I, 99.5%), lead iodide (PbI₂, 99.9%) and phenyl-C₆₁-butyric acid methyl ester (PCBM, 99.5%) were all acquired from Xi'an Polymer Light Technology Corp., China. The patterned fluorine-doped tin oxide (FTO)-coated glass substrates were purchased from Shanghai MaterWin New Materials Co., Ltd, China. Nickel foil (300 μm thickness, 99.99%) was purchased from Shengshida Metal Materials Co., Ltd, China. Isopropanol (IPA), dimethyl sulfoxide (DMSO, 99.8%), chlorobenzene (CB, 99.5%), γ -butyrolactone (GBL, 99.8%), polystyrene (PS, MW $\sim 190\,000$) and nickel nitrate (Ni(NO₃)₂·6H₂O, 99%) were all acquired from InnoChem, China.

4.2. Solution preparation

The perovskite precursor solution was prepared by dissolving CH₃NH₃I and PbI₂ (molar ratio = 1 : 1) in 1 mL mixed solvent of GBL and DMSO (7 : 3 v/v) with a molar concentration of 1 M. PS was dissolved in CB with concentrations of 0.2, 0.5, 1.0, 2.0, and 5.0 mg mL⁻¹. PCBM was also dissolved in chlorobenzene with a concentration of 20 mg mL⁻¹. Nickel nitrate was dissolved in deionized water with a molar concentration of 0.02 M.

4.3. Device fabrication

The patterned FTO/glass substrates were sequentially cleaned by sonication in acetone, isopropanol, ethanol and deionized water for 15 min at each step. The NiO_x mesoporous film was prepared by the electrochemical deposition (ECD) method using a programmable electrochemical workstation (CS350H, Corrtest, China) and the details can be found in our previous reports.^{14,39} For the bottom passivation layer, PS solutions with different concentrations were spin-coated on the NiO_x film at 4000 rpm for 30 s. Then the samples were annealed at 70 °C for 10 min on a hot plate. After that, the perovskite layer was grown by a one-step method in a nitrogen-filled glovebox. The perovskite precursor solution was spin-coated onto the passivation layer at 500 rpm for 12 s and then 4000 rpm for 30 s. For the top passivation layer, 150 μL PS solution was quickly dropped onto the perovskite precursor as the antisolvent 10 s before the end of

the spin-coating process. A control sample was prepared through the same procedure but using the pure CB solvent as the antisolvent. Subsequently, the samples were placed in an airtight glass pot and dried in a muffle furnace at 100 °C for 10 min. The PCBM solution was then spun onto the perovskite layer at 2000 rpm for 30 s. Each as-prepared solution was filtered through a polytetrafluoroethylene (PTFE) filter (0.45 μm) before the spin-coating process. Finally, approximately 120 nm thick silver electrodes were deposited on the top of the PCBM layer by thermal evaporation (PECVD350, Shenyang Xinlantian Vacuum Technology Co., Ltd, China). The active area of the PSC devices is 0.25 cm².

4.4. Characterization

The morphology of the samples was examined by scanning electron microscopy (SEM, Carl Zeiss, Germany) and atomic force microscopy (AFM, Nanoscope IIIa Multimode, USA). The transmission spectra of the NiO_x film and the absorption spectra of the perovskite layer were collected by using a UV/vis/NIR spectrophotometer (LAMBDA750, PerkinElmer, USA). The surface wettability of the prepared passivation layer was measured using a contact angle analyzer (DSA100, KRÜSS, Germany). The crystallinity of the perovskite film was characterized by X-ray diffraction (XRD, D8 ADVANCE, Germany). Furthermore, the steady-state photoluminescence (PL) and time-resolved photoluminescence (TRPL) spectra of the samples were measured using a steady-state & time-resolved fluorescence spectrofluorometer (QM/TM/IM, PTI, USA) with an excitation laser of 460 nm. The photocurrent density–voltage (*J*–*V*) curves of the as-fabricated devices were obtained under standard 1 sun AM 1.5G with a solar simulator (Newport, 2612A) in air, with a scanning rate of 0.1 V s⁻¹. The solar simulator was calibrated with a Newport 91 150 V reference silicon cell system before measurement. The external quantum efficiency (EQE) spectra of PSCs were measured using a quantum efficiency measurement system (QEX10, PV measurements, USA) in air without bias light. Electrochemical impedance spectroscopy (EIS) was carried out at a potential of 0.7 V in the dark with a frequency sweep from 1 Hz to 100 kHz using an electrochemical workstation (CS350H, Corrtest, China) and the oscillation potential amplitude was adjusted to 10 mV.

Conflicts of interest

The authors declare no conflict of interest.

Acknowledgements

This work was supported by the Natural Science Foundation of China (11834011, 11674225, 11474201, and 11204176).

References

- M. K. Assadi, S. Bakhoda, R. Saidur and H. Hanaei, *Renewable Sustainable Energy Rev.*, 2018, **81**, 2812–2822.
- A. B. Djurišić, F. Z. Liu, H. W. Tam, M. K. Wong, A. Ng, C. Surya, W. Chen and Z. B. He, *Prog. Quantum Electron.*, 2017, **53**, 1–37.
- Z. Wang, Q. Lin, B. Wenger, M. G. Christoforo, Y.-H. Lin, M. T. Klug, M. B. Johnston, L. M. Herz and H. J. Snaith, *Nat. Energy*, 2018, **3**, 855–861.
- N. J. Jeon, H. Na, E. H. Jung, T.-Y. Yang, Y. G. Lee, G. Kim, H.-W. Shin, S. Il Seok, J. Lee and J. Seo, *Nat. Energy*, 2018, **3**, 682–689.
- NREL, *Efficiency chart*, <https://www.nrel.gov/pv/assets/pdfs/best-research-cell-efficiencies-190416.pdf>, accessed April 2019.
- A. Rajagopal, K. Yao and A. K. Jen, *Adv. Mater.*, 2018, **30**, 1800455.
- Y. Wu, F. Xie, C. Han, X. Yang, H. Su, M. Cai, Z. Zhou, T. Noda and L. Han, *Adv. Mater.*, 2017, **29**, 1701073.
- K. Yao, F. Li, Q. He, X. Wang, Y. Jiang, H. Huang and A. K. Y. Jen, *Nano Energy*, 2017, **40**, 155–162.
- H. Zhang, J. Cheng, F. Lin, H. He, J. Mao, K. S. Wong, A. K. Jen and W. C. Choy, *ACS Nano*, 2015, **10**, 1503.
- Y. Hou, W. Chen, D. Baran, T. Stubhan, N. A. Luechinger, B. Hartmeier, M. Richter, J. Min, S. Chen, C. O. Quiroz, N. Li, H. Zhang, T. Heumueller, G. J. Matt, A. Osvet, K. Forberich, Z. G. Zhang, Y. Li, B. Winter, P. Schweizer, E. Spiecker and C. J. Brabec, *Adv. Mater.*, 2016, **28**, 5112–5120.
- T. Wang, D. Ding, X. Wang, R. Zeng, H. Liu and W. Shen, *ACS Omega*, 2018, **3**, 18434–18443.
- W. Chen, L. Xu, X. Feng, J. Jie and Z. He, *Adv. Mater.*, 2017, **29**, 1603923.
- W. Chen, Y. Zhou, L. Wang, Y. Wu, B. Tu, B. Yu, F. Liu, H. W. Tam, G. Wang, A. B. Djurisic, L. Huang and Z. He, *Adv. Mater.*, 2018, **30**, 1800515.
- Y. Bai, H. Chen, S. Xiao, Q. Xue, T. Zhang, Z. Zhu, Q. Li, C. Hu, Y. Yang, Z. Hu, F. Huang, K. S. Wong, H.-L. Yip and S. Yang, *Adv. Funct. Mater.*, 2016, **26**, 2950–2958.
- T. Leijtens, G. E. Eperon, N. K. Noel, S. N. Habisreutinger, A. Petrozza and H. J. Snaith, *Adv. Energy Mater.*, 2015, **5**, 1500963.
- D. Bi, C. Yi, J. Luo, J. D. Décoppet, F. Zhang, S. M. Zakeeruddin, X. Li, A. Hagfeldt and M. Grätzel, *Nat. Energy*, 2016, **1**, 16142.
- Y. Du, C. Xin, W. Huang, B. Shi, Y. Ding, C. Wei, Y. Zhao, Y. Li and X. Zhang, *ACS Sustainable Chem. Eng.*, 2018, **6**, 16806–16812.
- L. J. Tang, X. Chen, T. Y. Wen, S. Yang, J. J. Zhao, H. W. Qiao, Y. Hou and H. Yang, *Chem.–Eur. J.*, 2018, **24**, 2845–2849.
- Q. Wang, Q. Dong, T. Li, A. Gruverman and J. Huang, *Adv. Mater.*, 2016, **28**, 6734–6739.
- H. Zhang, J. Shi, L. Zhu, Y. Luo, D. Li, H. Wu and Q. Meng, *Nano Energy*, 2018, **43**, 383–392.
- Y. Zhao, Q. Li, W. Zhou, Y. Hou, Y. Zhao, R. Fu, D. Yu, X. Liu and Q. Zhao, *Sol. RRL*, 2019, **3**, 1800296.
- F. Zhang, J. Song, R. Hu, Y. Xiang, J. He, Y. Hao, J. Lian, B. Zhang, P. Zeng and J. Qu, *Small*, 2018, **14**, 1704007.
- H. Luo, S. Chen, L. Liu, X. Zhou, C. Ma, W. Liu and D. Zhang, *ACS Sustainable Chem. Eng.*, 2019, **7**, 3145–3153.

- 24 H. Luo, X. Zhou, C. Ellingford, Y. Zhang, S. Chen, K. Zhou, D. Zhang, C. R. Bowen and C. Wan, *Chem. Soc. Rev.*, 2019, **48**, 4424–4465.
- 25 J. Cao, B. Wu, R. Chen, Y. Wu, Y. Hui, B. W. Mao and N. Zheng, *Adv. Mater.*, 2018, **30**, 1705596.
- 26 Q. Jiang, Y. Zhao, X. Zhang, X. Yang, Y. Chen, Z. Chu, Q. Ye, X. Li, Z. Yin and J. You, *Nat. Photonics*, 2019, **13**, 460–466.
- 27 X. Bu, R. J. E. Westbrook, L. Lanzetta, D. Ding, T. Chotchuangchutchaval, N. Aristidou and S. A. Haque, *Sol. RRL*, 2019, **3**, 1800282.
- 28 J. Peng, J. I. Khan, W. Liu, E. Ugur, T. Duong, Y. Wu, H. Shen, K. Wang, H. Dang, E. Aydin, X. Yang, Y. Wan, K. J. Weber, K. R. Catchpole, F. Laquai, S. De Wolf and T. P. White, *Adv. Energy Mater.*, 2018, **8**, 1801208.
- 29 A. B. Huang, J. T. Zhu, J. Y. Zheng, Y. Yu, Y. Liu, S. W. Yang, S. H. Bao, L. Lei and P. Jin, *J. Mater. Chem. C*, 2016, **4**, 10839–10846.
- 30 Y. Wang, W. Fu, J. Yan, J. Chen, W. Yang and H. Chen, *J. Mater. Chem. A*, 2018, **6**, 13090–13095.
- 31 S. Sidhik, A. C. Pasarán, C. Rosiles Pérez, T. López-Luke and E. De la Rosa, *J. Mater. Chem. C*, 2018, **6**, 7880–7889.
- 32 F. Yang, H. E. Lim, F. Wang, M. Ozaki, A. Shimazaki, J. Liu, N. B. Mohamed, K. Shinokita, Y. Miyauchi, A. Wakamiya, Y. Murata and K. Matsuda, *Adv. Mater. Interfaces*, 2018, **5**, 1701256.
- 33 A. Trachtenberg, T. P. Vinod and R. Jelinek, *Polymer*, 2014, **55**, 5095–5101.
- 34 I. Hwang, I. Jeong, J. Lee, J. K. Min and K. Yong, *ACS Appl. Mater. Interfaces*, 2015, **7**, 17330.
- 35 F. Wang, W. J. Toe, W. M. Lee, D. McGloin, Q. Gao, H. H. Tan, C. Jagadish and P. J. Reece, *Nano Lett.*, 2013, **13**, 1185–1191.
- 36 J. Zhang, H. Luo, W. Xie, X. Lin, X. Hou, J. Zhou, S. Huang, W. Ou-Yang, Z. Sun and X. Chen, *Nanoscale*, 2018, **10**, 5617–5625.
- 37 L. Gao, S. Huang, L. Chen, X. Li, B. Ding, S. Huang and G. Yang, *Sol. RRL*, 2018, **2**, 1800088.
- 38 F. Wang, A. Shimazaki, F. Yang, K. Kanahashi, K. Matsuki, Y. Miyauchi, T. Takenobu, A. Wakamiya, Y. Murata and K. Matsuda, *J. Phys. Chem. C*, 2017, **121**, 1562–1568.
- 39 T. Wang, D. Ding, H. Zheng, X. Wang, J. Wang, H. Liu and W. Shen, *Sol. RRL*, 2019, **3**, 1900045.
- 40 A. K. Chandiran, N. Tetreault, R. Humphry-Baker, F. Kessler, E. Baranoff, C. Yi, M. K. Nazeeruddin and M. Grätzel, *Nano Lett.*, 2012, **12**, 3941–3947.
- 41 W. E. I. Sha, X. Ren, L. Chen and W. C. H. Choy, *Appl. Phys. Lett.*, 2015, **106**, 221104.
- 42 J. C. Yu, S. Badgujar, E. D. Jung, V. K. Singh, D. W. Kim, J. Gierschner, E. Lee, Y. S. Kim, S. Cho, M. S. Kwon and M. H. Song, *Adv. Mater.*, 2019, **31**, 1805554.
- 43 P. Zhao, B. J. Kim and H. S. Jung, *Materials Today Energy*, 2018, **7**, 267–286.
- 44 G. Liao, Z. Liu, B. Sun, X. Liu, J. Han, H. Ye, Y. Tu, C. Chen, T. Shi and Z. Tang, *J. Mater. Chem. A*, 2018, **6**, 7409–7419.
- 45 J. J. Peng, Y. N. Chen, K. B. Zheng, T. Pullerits and Z. Q. Liang, *Chem. Soc. Rev.*, 2017, **46**, 5714–5729.
- 46 J. Duan, Y. Zhao, X. Yang, Y. Wang, B. He and Q. Tang, *Adv. Energy Mater.*, 2018, **8**, 1802346.
- 47 S. S. Mali, H. Kim, H. H. Kim, E. S. Sang and K. H. Chang, *Mater. Today*, 2018, **21**, 483–500.
- 48 X. Yan, J. Zheng, L. L. Zheng, G. Lin, H. Lin, G. Chen, B. Du and F. Zhang, *Mater. Res. Bull.*, 2018, **103**, 150–157.